Stability in computed optical interferometric tomography (Part II): *in vivo* stability assessment

Nathan D. Shemonski,[1,2] Adeel Ahmad,[1,2] Steven G. Adie,[3] Yuan-Zhi Liu,[1,2] Fredrick A. South,[1,2] P. Scott Carney,[1,2] and Stephen A. Boppart[1,2,4,*]

[1]*Beckman Institute for Advanced Science and Technology, University of Illinois at Urbana-Champaign, USA*
[2]*Department of Electrical and Computer Engineering, University of Illinois at Urbana-Champaign, USA*
[3]*Department of Biomedical Engineering, Cornell University, USA*
[4]*Departments of Bioengineering and Internal Medicine, University of Illinois at Urbana-Champaign, USA*
[*]*boppart@illinois.edu*

Abstract: Stability is of utmost importance to a wide range of phase-sensitive processing techniques. In Doppler optical coherence tomography and optical coherence elastography, in addition to defocus and aberration correction techniques such as interferometric synthetic aperture microscopy and computational/digital adaptive optics, a precise understanding of the system and sample stability helps to guide the system design and choice of imaging parameters. This article focuses on methods to accurately and quantitatively measure the stability of an imaging configuration *in vivo*. These methods are capable of partially decoupling axial from transverse motion and are compared against the stability requirements for computed optical interferometric tomography laid out in the first part of this article.

References and links

1. V. X. D. Yang, M. L. Gordon, B. Qi, J. Pekar, S. Lo, E. Seng-Yue, A. Mok, B. C. Wilson, and I. A. Vitkin, "High speed, wide velocity dynamic range Doppler optical coherence tomography (Part I): System design, signal processing, and performance," Opt. Express **11**(7), 794–809 (2003).
2. V. X. D. Yang, M. L. Gordon, E. Seng-Yue, S. Lo, B. Qi, J. Pekar, A. Mok, B. C. Wilson, and I. A. Vitkin, "High speed, wide velocity dynamic range Doppler optical coherence tomography (Part II): Imaging *in vivo* cardiac dynamics of *Xenopus laevis*," Opt. Express **11**(14), 1650–1658 (2003).
3. R. K. Wang, S. L. Jacques, Z. Ma, S. Hurst, S. R. Hanson, and A. Gruber, "Three dimensional optical angiography," Opt. Express **15**(7), 4083–4097 (2007).
4. J. Fingler, R. J. Zawadzki, J. S. Werner, D. Schwartz, and S. E. Fraser, "Volumetric microvascular imaging of human retina using optical coherence tomography with a novel motion contrast technique," Opt. Express **17**(24), 22190–22200 (2009).
5. A. L. Oldenburg, F. J. J. Toublan, K. S. Suslick, A. Wei, and S. A. Boppart, "Magnetomotive contrast for *in vivo* optical coherence tomography," Opt. Express **13**(17), 6597–6614 (2005).
6. C. Joo, T. Akkin, B. Cense, B. H. Park, and J. F. de Boer, "Spectral-domain optical coherence phase microscopy for quantitative phase-contrast imaging," Opt. Lett. **30**(16), 2131–2133 (2005).
7. W. Qi, R. Chen, L. Chou, G. Liu, J. Zhang, Q. Zhou, and Z. Chen, "Phase-resolved acoustic radiation force optical coherence elastography," J. Biomed. Opt. **17**(11), 110505 (2012).
8. V. Crecea, A. L. Oldenburg, X. Liang, T. S. Ralston, and S. A. Boppart, "Magnetomotive nanoparticle transducers for optical rheology of viscoelastic materials," Opt. Express **17**(25), 23114–23122 (2009).
9. V. Crecea, A. Ahmad, and S. A. Boppart, "Magnetomotive optical coherence elastography for microrheology of biological tissues," J. Biomed. Opt. **18**(12), 121504 (2013).
10. C. Dorronsoro, D. Pascual, P. Pérez-Merino, S. Kling, and S. Marcos, "Dynamic OCT measurement of corneal deformation by an air puff in normal and cross-linked corneas," Biomed. Opt. Express **3**(3), 473–487 (2012).
11. T. S. Ralston, D. L. Marks, P. S. Carney, and S. A. Boppart, "Interferometric synthetic aperture microscopy," Nat. Phys. **3**(2), 129–134 (2007).

12. B. J. Davis, S. C. Schlachter, D. L. Marks, T. S. Ralston, S. A. Boppart, and P. S. Carney, "Non-paraxial vector-field modeling of optical coherence tomography and interferometric synthetic aperture microscopy," J. Opt. Soc. Am. A **24**(9), 2527–2542 (2007).
13. B. J. Davis, D. L. Marks, T. S. Ralston, P. S. Carney, and S. A. Boppart, "Interferometric synthetic aperture microscopy: computed imaging for scanned coherent microscopy," Sensors (Basel) **8**(6), 3903–3931 (2008).
14. S. G. Adie, B. W. Graf, A. Ahmad, P. S. Carney, and S. A. Boppart, "Computational adaptive optics for broadband optical interferometric tomography of biological tissue," Proc. Natl. Acad. Sci. U.S.A. **109**(19), 7175–7180 (2012).
15. S. G. Adie, N. D. Shemonski, B. W. Graf, A. Ahmad, P. Scott Carney, and S. A. Boppart, "Guide-star-based computational adaptive optics for broadband interferometric tomography," Appl. Phys. Lett. **101**(22), 221117 (2012).
16. A. Kumar, W. Drexler, and R. A. Leitgeb, "Subaperture correlation based digital adaptive optics for full field optical coherence tomography," Opt. Express **21**(9), 10850–10866 (2013).
17. D. Hillmann, C. Lührs, T. Bonin, P. Koch, and G. Hüttmann, "Holoscopy--holographic optical coherence tomography," Opt. Lett. **36**(13), 2390–2392 (2011).
18. D. Hillmann, G. Franke, C. Lührs, P. Koch, and G. Hüttmann, "Efficient holoscopy image reconstruction," Opt. Express **20**(19), 21247–21263 (2012).
19. N. D. Shemonski, S. G. Adie, Y.-Z. L. F. A. South, P. S. Carney, and S. A. Boppart, "Stability in computed optical interferometric tomography (Part I): Stability requirements,"(to be published).
20. W. Choi, B. Potsaid, V. Jayaraman, B. Baumann, I. Grulkowski, J. J. Liu, C. D. Lu, A. E. Cable, D. Huang, J. S. Duker, and J. G. Fujimoto, "Phase-sensitive swept-source optical coherence tomography imaging of the human retina with a vertical cavity surface-emitting laser light source," Opt. Lett. **38**(3), 338–340 (2013).
21. T. S. Ralston, D. L. Marks, P. S. Carney, and S. A. Boppart, "Phase stability technique for inverse scattering in optical coherence tomography," in *Proceedings of 3rd IEEE International Symposium on Biomedical Imaging: Nano to Macro* (2006), pp. 578–581.
22. C. Sun, F. Nolte, K. H. Y. Cheng, B. Vuong, K. K. C. Lee, B. A. Standish, B. Courtney, T. R. Marotta, A. Mariampillai, and V. X. D. Yang, "*In vivo* feasibility of endovascular Doppler optical coherence tomography," Biomed. Opt. Express **3**(10), 2600–2610 (2012).
23. M.-T. Tsai, T.-T. Chi, H.-L. Liu, F.-Y. Chang, C.-H. Yang, C.-K. Lee, and C.-C. Yang, "Microvascular imaging using swept-source optical coherence tomography with single-channel acquisition," Appl. Phys. Express **4**(9), 097001 (2011).
24. M. Pircher, B. Baumann, E. Götzinger, H. Sattmann, and C. K. Hitzenberger, "Phase contrast coherence microscopy based on transverse scanning," Opt. Lett. **34**(12), 1750–1752 (2009).
25. M. A. Choma, A. K. Ellerbee, C. Yang, T. L. Creazzo, and J. A. Izatt, "Spectral-domain phase microscopy," Opt. Lett. **30**(10), 1162–1164 (2005).
26. M. V. Sarunic, S. Weinberg, and J. A. Izatt, "Full-field swept-source phase microscopy," Opt. Lett. **31**(10), 1462–1464 (2006).
27. T. S. Ralston, D. L. Marks, P. S. Carney, and S. A. Boppart, "Inverse scattering for optical coherence tomography," J. Opt. Soc. Am. A **23**(5), 1027–1037 (2006).
28. V. J. Srinivasan, S. Sakadžić, I. Gorczynska, S. Ruvinskaya, W. Wu, J. G. Fujimoto, and D. A. Boas, "Quantitative cerebral blood flow with optical coherence tomography," Opt. Express **18**(3), 2477–2494 (2010).
29. B. J. Vakoc, G. J. Tearney, and B. E. Bouma, "Statistical properties of phase-decorrelation in phase-resolved Doppler optical coherence tomography," IEEE Trans. Med. Imaging **28**(6), 814–821 (2009).
30. B. H. Park, M. C. Pierce, B. Cense, S.-H. Yun, M. Mujat, G. J. Tearney, B. E. Bouma, and J. F. de Boer, "Real-time fiber-based multi-functional spectral-domain optical coherence tomography at 1.3 µm," Opt. Express **13**(11), 3931–3944 (2005).
31. B. Braaf, K. A. Vermeer, K. V. Vienola, and J. F. de Boer, "Angiography of the retina and the choroid with phase-resolved OCT using interval-optimized backstitched B-scans," Opt. Express **20**(18), 20516–20534 (2012).
32. J. Lee, V. Srinivasan, H. Radhakrishnan, and D. A. Boas, "Motion correction for phase-resolved dynamic optical coherence tomography imaging of rodent cerebral cortex," Opt. Express **19**(22), 21258–21270 (2011).
33. B. R. White, M. C. Pierce, N. Nassif, B. Cense, B. H. Park, G. J. Tearney, B. E. Bouma, T. C. Chen, and J. F. de Boer, "*In vivo* dynamic human retinal blood flow imaging using ultra-high-speed spectral domain optical coherence tomography," Opt. Express **11**(25), 3490–3497 (2003).
34. X. Liu, Y. Huang, and J. U. Kang, "Distortion-free freehand-scanning OCT implemented with real-time scanning speed variance correction," Opt. Express **20**(15), 16567–16583 (2012).
35. A. Ahmad, S. G. Adie, E. J. Chaney, U. Sharma, and S. A. Boppart, "Cross-correlation-based image acquisition technique for manually-scanned optical coherence tomography," Opt. Express **17**(10), 8125–8136 (2009).
36. X. Liu, J. C. Ramella-Roman, Y. Huang, Y. Guo, and J. U. Kang, "Robust spectral-domain optical coherence tomography speckle model and its cross-correlation coefficient analysis," J. Opt. Soc. Am. A **30**(1), 51–59 (2013).
37. B. W. Graf, S. G. Adie, and S. A. Boppart, "Correction of coherence gate curvature in high numerical aperture optical coherence imaging," Opt. Lett. **35**(18), 3120–3122 (2010).
38. A. Ahmad, N. D. Shemonski, S. G. Adie, H.-S. Kim, W.-M. W. Hwu, P. S. Carney, and S. A. Boppart, "Real-time *in vivo* computed optical interferometric tomography," Nat. Photonics **7**(6), 444–448 (2013).

39. B. Považay, B. Hofer, C. Torti, B. Hermann, A. R. Tumlinson, M. Esmaeelpour, C. A. Egan, A. C. Bird, and W. Drexler, "Impact of enhanced resolution, speed and penetration on three-dimensional retinal optical coherence tomography," Opt. Express **17**(5), 4134–4150 (2009).

1. Introduction

Phase sensitive processing techniques such as Doppler optical coherence tomography (OCT) [1, 2], optical micro-angiography (OMAG) [3], phase variance OCT [4], magnetomotive OCT [5], quantitative optical phase microscopy [6], in addition to elastography techniques such as acoustic radiation force (ARF) optical coherence elastography (OCE) [7], magnetomotive OCE [8, 9], air puff OCE [10], and computed optical interferometric techniques such as interferometric synthetic aperture microscopy (ISAM) [11–13], computational adaptive optics (CAO) [14, 15], digital adaptive optics (DAO) [16], and holoscopy [17, 18] all share the common requirement of stability. The phase quantity used in these techniques is not only sensitive to transverse motion of the sample, but is highly sensitive to axial motion as was discussed in the first part of this paper [19]. The sensitivity to axial motion is a commonly known property of coherent imaging modalities, and is often utilized to measure sub-wavelength displacements [1, 4, 5].

Currently, stability (often referred to as 'phase stability') can be assessed by a variety of techniques, but is often not reported in the literature when describing the system performance specifications. The simplest is by use of a mirror or partial reflector placed at the focus of the beam in the sample arm from which sequential M-mode or B-mode data are acquired and analyzed [20–26]. Though simple, a stability assessment using a partial reflector is an important measurement to make for any phase sensitive system, as the results can be compared with the expected theoretical performance to ensure the source and/or reference arm are not limiting factors to stability or significant contributors to noise in the system. The use of a mirror or partial reflector allows one to determine the lowest signal-to-noise ratio (SNR) from which phase data can be reliably measured. It is understood that one's ability to determine the phase from an OCT signal is strongly dependent on the SNR. Although the SNR dependence of phase stability has an immediate impact on most phase-based techniques, as discussed in the first part of this article [19] and demonstrated in other reports [27], computed optical interferometric techniques can be very robust to even low levels of SNR.

Most analyses end here quoting only a single number for the phase stability of a system, however, a broader range of instabilities are present in optical systems which are equally important to consider but cannot be easily measured using a partial reflector. These include instabilities such as those from the scanning optics and most types of sample motion. In addition, the use of a partial reflector is not compatible with some system geometries such as rotational motion in catheters or endoscopes. This motivates the need for a more general stability assessment which can complement this current standard measure of stability.

In other studies, stability assessments have been performed by scanning/imaging a controlled tissue phantom (often uniformly scattering) [1, 22] in an attempt to measure a wider range of instabilities such as scanning jitter or irregularities [22, 28]. These methods are typically used after the source and reference arm have been confirmed to be acceptably stable using a mirror or partial reflector. As discussed in [29, 30], the phase changes due to transverse motion are dependent on the numerical aperture (NA) and resolution of the imaging system. This means that especially for high-NA imaging systems, jitter in the scanning system could be the limiting factor in phase determination and stability.

Although using a known tissue phantom provides a somewhat realistic imaging scenario, one can still move toward more complex samples and scenarios. Perhaps the most general method of stability assessment is to include the particular sample of interest in the measurement of stability [31, 32]. This is particularly useful for *in vivo* imaging where sample motion is often the limiting stability factor. Ideally, during this assessment, the system is operated in the exact same way as if it was acquiring an image. That way, all possible

instabilities are present and can be fully detected and characterized. Though some investigations have used the sample of interest for stability assessments, they have typically only been concerned with the general phase difference statistics. For the computed imaging techniques discussed here, both the amplitude and phase are used for reconstructions and thus we desire a more thorough investigation where quantitative displacements (ideally in all three dimensions) are physically measured. By quantifying the types of motion/instabilities which influence our measurements, more informed system designs and imaging parameter choices can be made. This way, the effects of motion on reconstructions can be avoided to reduce the need for post-processed corrections where possible.

2. Multidimensional stability assessment

In the first part of this paper [19], we set forth guidelines which provided the stability requirements for computational defocus and aberration correction techniques. We found that a single number could not be assigned to ensure stability for aberration correction techniques due to the complex, non-linear relationship between motion and computational reconstructions. Instead, our strategy was, given knowledge of the type and amount of motion in the axial and transverse dimensions, one could predict how well aberration correction would work. This section seeks to set forth a strategy to appropriately assess the stability of a system and sample for the purpose of computational defocus and aberration correction.

2.1 Background theory

The method laid out here combines two separate analysis techniques. The first relies primarily on the phase of the acquired signal, while the second relies only on the amplitude. The separation is natural for our stability analysis as optical path length (OPL) fluctuations and axial motion manifest predominantly as phase changes. Alternatively, scanning jitter or transverse motion manifest somewhat equally between phase and amplitude instabilities.

We begin with the phase analysis. The phase at any given point in an OCT tomogram is directly related to the phase of the backscattered light collected from the sample. Thus, if phase differences are calculated at the same point over time, an OPL change, Δz, results in a phase change, $\Delta \phi$, according to

$$\Delta \phi = 2 n_{\text{sample}} k_0 \Delta z \qquad (1)$$

Where n_{sample} is the overall refractive index of the material and $k_0 = 2\pi / \lambda_0$ is the optical wave number in air, and λ_0 is the central wavelength in air. The factor of 2 is due to the typical double-pass configuration in OCT. Transverse motion also affects this phase change, but in a less predictable manner. As was previously calculated [29], the phase changes due to transverse motion are random with a predictable probability distribution function (pdf). Most importantly, the pdf is mean zero. Let $\Delta \omega(z)$ be the random phase changes as a function of depth due to transverse motion. Then the total phase change along a given depth can be written as $\Delta \phi(z) = 2 n_{\text{sample}} k_0 \Delta z + \Delta \omega(z)$. Thus, by averaging $\Delta \phi(z)$ over depth, transverse motion can be eliminated, preserving only bulk OPL changes. This analysis is similar to the stabilization techniques previously used in Dopper OCT [33].

The next technique uses the amplitude of the acquired data to analyze larger-scale motion. We begin with a result relating speckle decorrelation to physical displacements. According to previous studies involving manual scanning [34–36], transverse movement along one direction can be related to the cross correlation coefficient (XCC) according to $\Delta x = w_{1/e} \sqrt{\ln\left(1/\rho\right)}$ where ρ is the XCC between two A-scans before and after movement, $w_{1/e}$ is the 1/e mark of the Gaussian point spread function (PSF), and Δx is the magnitude of

the displacement along that dimension. We note that for the XCC analysis, it is more natural to work with the $1/e$ point of the Gaussian PSF while elsewhere we use the $1/e^2$ point.

In the manual scanning techniques, motion is restricted to a single dimension. When motion is possible in all three dimensions and if the resolution is isotropic, then the result becomes

$$\| \Delta r \| = w_{1/e} \sqrt{\ln\left(1/\rho\right)} \tag{2}$$

where Δr is the 3-D movement vector between A-scans. For OCT, though, there is typically a discrepancy between the axial (w_z) and transverse ($w_\parallel$) resolution. Then, the XCC can be decomposed into $\rho = \rho_\parallel + \rho_z$ where $\rho_\parallel = \exp\left(-\| \Delta r_\parallel \|^2 / w_\parallel^2\right)$ and $\rho_z = \exp\left(-\| \Delta z \|^2 / w_z^2\right)$. Thus, given knowledge of the axial motion from the phase analysis previously discussed, the influence of the axial motion on the XCC can be removed. Often though, the axial motion that can be tolerated by the computed imaging techniques considered here is small enough such that its contribution to the XCC is typically negligible.

Together, the above two techniques rely on the following three assumptions.

1. The sample being imaged provides fully-developed speckle at relatively uniform intensity over a depth range of approximately 50 depth resolution elements or more.

2. Any optical path length change (e.g. due to sample or reference arm motion) between two adjacent A-scans remains less than $\lambda_0 / 2$.

3. The magnitude of the motion vector in all three dimensions between two adjacent A-scans remains less than $w_{1/e} / 2$.
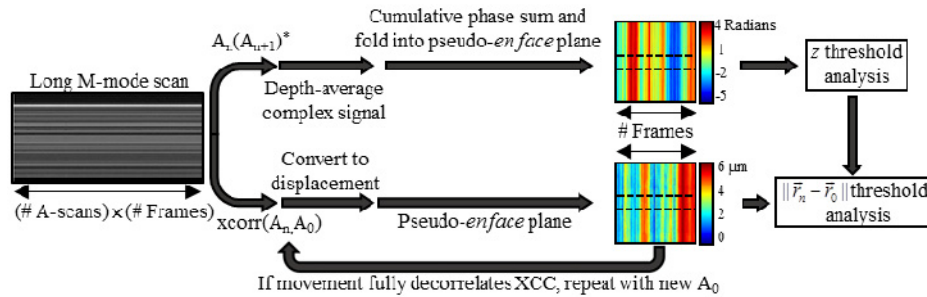
Fig. 1. Flow chart providing details for stability analysis. A single M-mode scan is used for two sets of analyses. The top path utilizes phase differences between adjacent A-scans to measure axial phase fluctuations. The bottom path utilizes the amplitude-based XCC between adjacent A-scans to measure motion on a larger scale.

The first assumption ensures that the XCC analysis can predict displacement distances as well as ensuring there is enough depth information to average over to cancel out the phase fluctuations from transverse motion. In addition, a relatively uniform scattering intensity will ensure that a single depth does not dominate the analysis. Due to the highly scattering nature of many biological tissues, this assumption is often met. The second and third assumptions ensure that the displacements are not too large since the phase analysis is prone to phase wrapping and the XCC is only reliable to a fraction of the PSF width [35].

2.2 General procedure

The procedure for stability analysis is depicted in Fig. 1. It begins with an M-mode scan where the imaging beam is held in one location. The M-mode scan should have the same number of A-scans as a full volume of data. Now following the top path of Fig. 1, we perform

the phase analysis using the complex data as obtained by standard spectral domain OCT processing steps (resampling, dispersion compensation and FFT). Phase differences are calculated via complex conjugate multiplication of adjacent A-scans: $A_i(A_{i+1})^*$. Next, the complex data is averaged over depth, resulting in a weighted circular mean. This naturally performs a weighted average ensuring that high SNR portions which provide more reliable phase information are weighted more. The weighted average can be understood from a vector-addition viewpoint where the SNR at each voxel corresponds to the length of a vector. Thus, small magnitude (low SNR) vectors will contribute little when added to large magnitude (high SNR) vectors. This is desirable as, in depth, there will be alternating bright and dark regions resulting from the speckle. It also alleviates some of the phase unwrapping steps performed in other analyses [33]. Now, the phase is extracted from the complex data and a cumulative sum is performed across time to convert the incremental phase changes to total phase changes relative to the initial time. In addition, the data set is rearranged as if a volume of data was raster-scanned and an *en face* plane was extracted. This 2-D plane provides two axes, a fast axis along which points were measured very closely in time, and a slow axis along which points were measured further apart in time. We call this 2-D plane a pseudo-*en face* plane because it was not acquired with a scanning beam. This 2-D map of phase fluctuations corresponds to axial displacements [following Eq. (1)] which occurred during imaging.

We can now compare the changes in *z* (axial displacements) to the threshold graphs laid out in Fig. 4 from the first part of this paper [19]. The thresholds are presented in a manner such that the axial changes should be analyzed along the slow axis. Thus, we take a thin strip down the middle of the pseudo-*en face* plane, average along the pseudo-fast axis, and use the resulting trace along the pseudo-slow axis. Comparing the level of Brownian motion, instantaneous steps, or dominant periodic motion along this trace to the levels presented in the threshold graphs in [19], one can understand how stable the axial changes are and if the configuration is sufficiently stable for the computed imaging techniques.

If the phase analysis proved the system to be stable, one can now move to the XCC stability analysis, which analyzes predominantly the transverse motion, since the axial motion was small. It begins with the same M-mode scan used in the phase analysis but now computes XCCs using only the amplitude data. First, the central A-scan from the M-mode scan is extracted, A_0, and the XCC between this scan and all other scans is computed, that provides $\|\vec{r}_n - \vec{r}_0\|$ where $\vec{r}_0$ is the position of the selected A-scan (A_0) and $\vec{r}_n$ is the position of the n$^{\text{th}}$ A-scan. Using Eq. (2), the XCCs can be converted to physical displacements and the pseudo-*en face* plane is extracted in a similar manner as in the phase analysis. To compare the displacements to Fig. 4 from [19], a central strip is again averaged along the pseudo-fast axis to obtain data along the pseudo-slow axis. The averaging here is important because the XCC analysis can be oscillatory and noisy at times. For the XCC results here, the entire fast axis was averaged. The flow chart in Fig. 1 also shows that the phase analysis can feed into the analysis of $\|\vec{r}_n - \vec{r}_0\|$. This should be taken into account if the axial displacements are large enough to be seen in the XCC analysis. The large axial displacements can be partially removed by taking into account the decomposition $\rho = \rho_\| + \rho_z$ discussed previously. Typically, though, the axial displacements tolerable to the computed imaging techniques are below the sensitivity displacement of the XCC analysis. A similar comparison of the Brownian motion, instantaneous steps, and sinusoidal motion to the thresholds graphs can then be performed.

We finally note that the XCC analysis will saturate after too much transverse motion due to a full decorrelation of the two scans. We find this to be about half the full width of the PSF, which agrees with previous studies [35, 36]. Thus, if the XCC analysis reveals motion larger than this distance, a new A-scan for A_0 should be chosen. If a single A-scan does not suffice,

a piecewise analysis along the slow axis may be necessary, though this implies that there may be too much motion for the computed imaging techniques to tolerate. Another technicality is that the XCC analysis provides the magnitude of displacements along all three dimensions relative to a single scan, as opposed to the absolute position. Therefore, the standard deviation of the XCC analysis may be different than the Brownian motion of the sample/system. Consider a 1-D Brownian motion process with increments of standard deviation given by σ. The XCC analysis then measures $|r_n - r_0|$ such that

$$\mathcal{P}\{|r_n - r_0|\} = \mathcal{N}_f(0, \mathrm{n}\,\sigma^2) \tag{3}$$

Where r_0 is the position of the selected A-scan (A_0), r_n is the position of the $\mathrm{n^{th}}$ A-scan, $\mathcal{P}\{x\}$ denotes the probability that the value x occurs, and $\mathcal{N}_f(0, \sigma^2)$ denotes a half-normal distribution resulting from a normal distribution with mean 0 and variance σ^2. Numerical simulations then show that, by looking at the incremental changes, $\mathrm{Std}\{|r_{n+1} - r_0| - |r_n - r_0|\} \approx \sigma$ where $\mathrm{Std}\{X\}$ is the standard deviation of X. Therefore, the standard deviation of the increments of our XCC analysis will provide us with the standard deviation of the underlying 1-D Brownian motion.

3. Experimental results

This section outlines a number of experiments showing the usability of the procedure outlined in Section 2. We begin with a proof-of-concept experiment followed by phantom and fixed tissue studies, and finally apply the procedure to *in vivo* imaging.

3.1 Procedure validation

As a proof-of-concept study, Fig. 2 shows results from imaging a phantom consisting of several layers of Scotch brand Magic Tape. A galvanometer scanner was placed in the reference arm for later studies. Figure 2(a) provides a baseline stability analysis where the reference arm galvanometer was held at one location during the M-mode imaging. Much of the jitter present in the phase analysis is due to the scanner in the reference arm. Next, to show the ability of this technique to detect small displacements, transverse and axial motion was induced in a controlled manner while M-mode imaging. The scale of these disturbances was chosen to be large enough such that the computed imaging techniques should begin to show artifacts, but small enough to show the appropriate sensitivity of the techniques. In Fig. 2(b), the scanner in the reference arm was varied during M-mode imaging to provide pure OPL variations. The measured and predicted traces are shown in both the phase and XCC analyses. Due to the magnitude of the OPL displacements, there was minor cross-talk into the XCC analysis. Figure 2(c) shows an experiment where the imaging beam was randomly scanned along a single axis. This is meant to simulate both sample motion and galvanometer scanner jitter. The sample was flattened with a coverslip to ensure that any transverse motion would not result in OPL changes. The XCC analysis shows the measured displacement and the applied displacement. For the phase analysis in Fig. 2(c), the averaging along the depth should remove all phase fluctuations due to transverse motion, and thus we expect to measure close to zero displacement. Finally, Fig. 2(d) shows the results where both the scanner in the reference arm and the beam were scanned with different patterns. In Figs. 2(b)–2(d), the phase analysis plots show the measured OPL displacement and the applied (expected) axial displacement while the XCC analysis shows the measured displacement and the applied (expected) transverse beam displacement. This experiment demonstrates the ability to separate axial from transverse motion as long as the axial motion is sufficiently small.
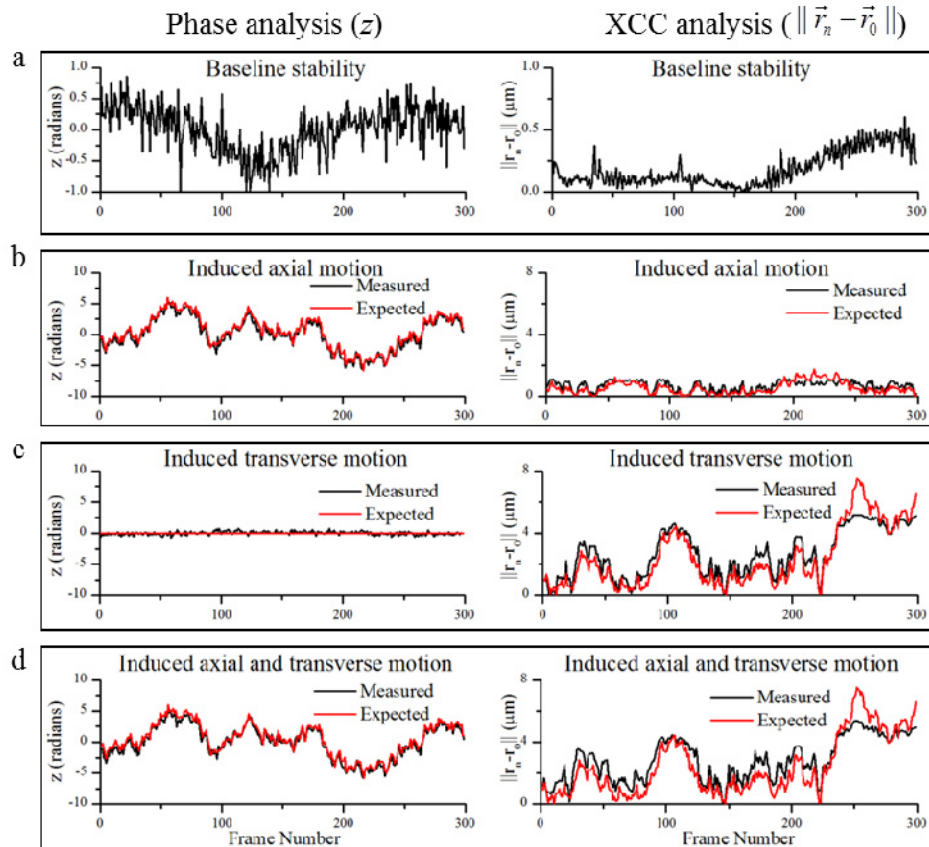
Fig. 2. Validating phase and XCC measurements. The left column shows the phase analysis which measures pure axial motion and the right column shows the XCC analysis which measured motion in all three dimensions. (a) Baseline stability measurements are made to provide a reference scale for the other figures. (b) Axial motion was induced by changing the OPL in the reference arm. With knowledge of the induced motion, both the measured and expected values are plotted for the phase and XCC analysis. This shows that for sufficiently large axial motion, the motion is also measured with the XCC analysis. (c) Transverse motion was induced by jittering the scanning galvanometer mirrors. As this represents almost purely transverse motion, the phase analysis should measure displacements close to the baseline measured in (a). (d) Motion is induced by both the reference arm and scanning mirrors. Since the axial motion is much smaller than the transverse, the XCC analysis measures mostly transverse motion while the phase analysis still only measures the axial motion.

3.2 Phantom and ex vivo tissue assessment

To experimentally validate the stability assessment set forth in Section 2.2, we performed controlled experiments with both a tissue phantom and fresh *ex vivo* healthy human breast tissue. Experiments were performed on a high-NA (0.6) fiber-based spectral-domain (SD) OCT system. Centered at 860 nm, a superluminescent diode (SLD) with a bandwidth of 80 nm (FWHM) was used, providing an axial resolution of 4.1 μm (FWHM) in air. Although the non-telecentric setup inherently has some coherence curvature [37], curvature was minimized by imaging the pivot from a pair of galvanometer scanning mirrors (Cambridge Technology) to the objective lens (Olympus, LUCPLFLN40X, NA = 0.6) and additional curvature was computationally corrected similar to the procedure outlined in [37]. This was performed using a collimating lens (f = 11 mm), scan lens (f = 75 mm), and tube lens (f = 180 mm, Olympus U-TLUIR). The resulting transverse resolution was measured to be 0.6 μm (FWHM). Detection was performed with a spectrometer (Bayspec, Inc.) using a 4096 pixel line-scan

camera (Basler, spL4096-140km) which was synchronized to the scanning mirrors using a camera link card (National Instruments, NI-PCIe 1427) and data acquisition card (National Instruments, NI-PCIe-6353). LabVIEW was used for the graphical user interface and data was processed via DLL calls to CUDA code running on a GPU (GeForce GTX 580, NVIDIA). Finally, an inverted microscope configuration was utilized for imaging *ex vivo* samples, which provided a reliable, clean, and flat surface for imaging.
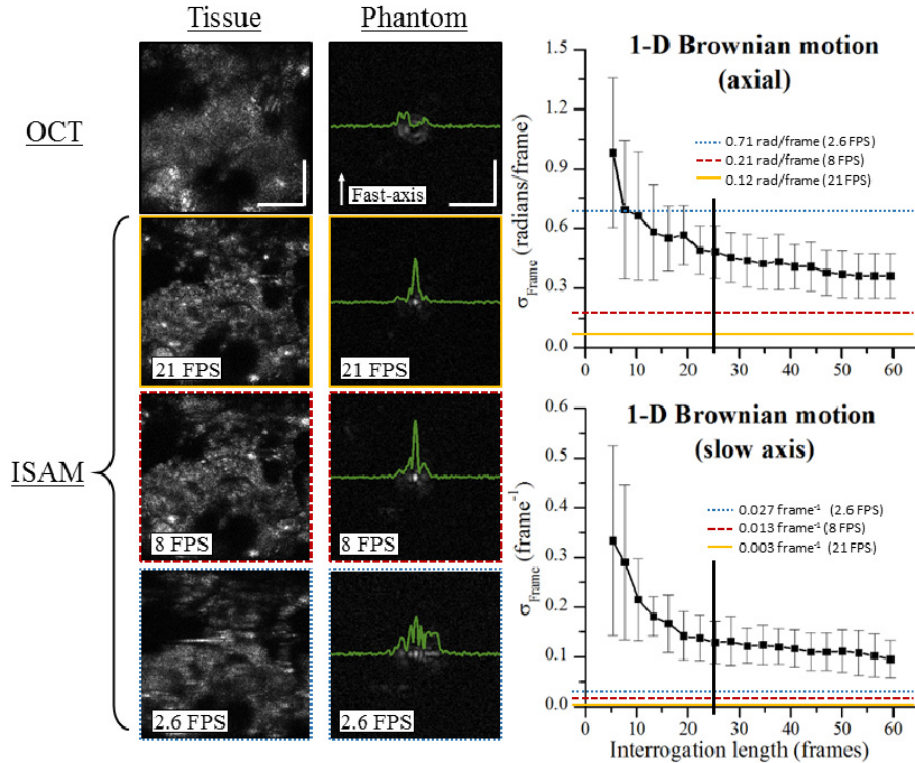
Fig. 3. Stability analysis for *ex vivo* tissues. The analysis procedure detailed in Fig. 1 is utilized to measure the stability of static samples. A tape phantom was used as the speckle-generating sample for stability measurement at three speeds: 21, 8, and 2.6 FPS. The plots on the right show colored/dashed lines which correspond to the resulting stability assessment. The colors and dash-type match the *en face* planes on the left with the same color/dash outline. The plots show that 21 and 8 FPS satisfy the stability requirements from [19], but at 2.6 FPS, motion is too great and predicts that reconstructions will no longer work. The vertical black line in the plots on the right indicates approximately the interrogation length for the phantom images. On the left, OCT and ISAM *en face* planes from both *ex vivo* breast tissue and a tissue phantom are shown. The reconstructions are seen to properly correct defocus at 21 and 8 FPS, but deteriorate at the slow, 2.6 FPS imaging speed. Scale bars in the phantom represent 10 μm and in the breast tissue represent 85 μm.

Experimentally, a tissue phantom consisting of sub-resolution TiO_2 particles in a clear 3-D silicone matrix was imaged at the same location at a variety of speeds. The same out-of-focus particle was then isolated and viewed from each 3-D tomogram. The *ex vivo* breast tissue was imaged on a separate day, though stability assessments were again performed to ensure a similar state of the system. The full field-of-view is shown for the breast tissue.

The results are presented in Fig. 3. On the left are the representative OCT data along with the ISAM reconstructions at each speed for both the tissue and phantom samples. The reconstructions at 21 frames per second (FPS) and 8 FPS appear typical for reconstructions on this system, with slightly larger side lobes in the 8 FPS reconstruction. The reconstruction

with the slowest imaging speed (2.6 FPS) shows strong motion artifacts along the slow axis, similar to those seen in Fig. 2 in Part I of this article [19].
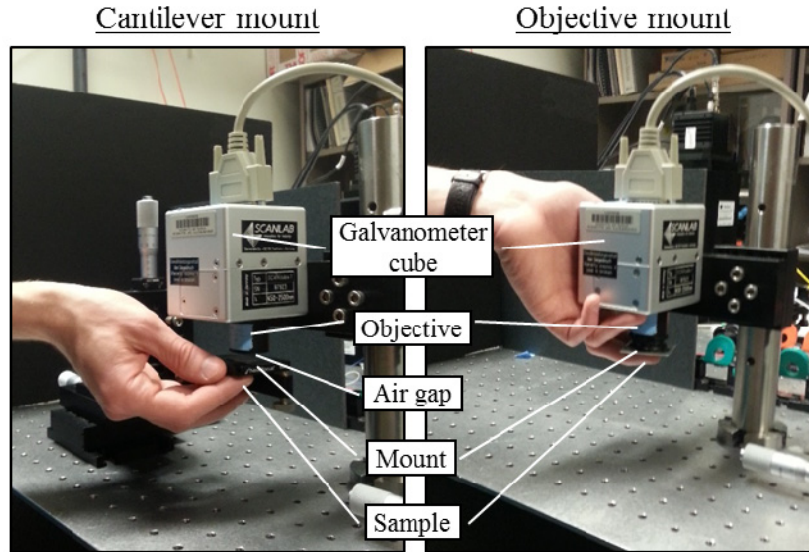
Fig. 4. Photographs of two *in vivo* tissue mounting systems. Pictured on the left is a cantilever mount (note 3-axis stage on table) where the sample and mount are separate from the rest of the sample arm optics (as indicated by the air gap). On the right is a monolithic, objective-mounted design where the sample mount is attached to objective lens tube. In the objective-mounted configuration, the optics and sample will move together providing a more stable configuration.

To quantitatively assess the stability of this system, the same static tape phantom from Section 3.1 was imaged (in M-mode) at the same three effective speeds (21 FPS, 8 FPS, and 2.6 FPS). The in-focus region was isolated and the process outlined in Fig. 1 was followed to extract the axial and transverse fluctuations. It was then assumed that these fluctuations can be modeled as a random walk (1-D Brownian motion). Thus the standard deviations of the incremental changes were calculated as the stability measure of the motion in the axial and transverse directions. Shown on the right side of Fig. 3 are the two relevant stability threshold plots from Fig. 4 in Part I of this article [19]. Although we cannot be sure that the transverse motion was only along the slow axis, Part I of this article showed that the thresholds along the slow axis are stricter than that of the fast axis. Thus, as a conservative measure, the slow-axis threshold plot was used. Overlaid on these plots, are lines showing the stability measurements (from the tape phantom) at each scan speed. The color and type of dashed lines correspond to the different imaging speeds used for the tissue and point-scattering phantom imaging. The estimated interrogation length for the ISAM reconstructions is indicated by the black vertical lines (~25 frames). At the intersection of these lines, we see that the stability assessment predicts successful ISAM reconstructions for 21 FPS and 8 FPS since the intersection points are below the threshold line. In addition, the analysis predicted that the ISAM reconstruction would be unsuccessful at 2.6 FPS, as the intersection points lay close or above the threshold lines.

3.3 *In vivo* assessment

To show the applicability of these techniques to *in vivo* imaging, a finger from a human volunteer was imaged with the system described in [38]. Briefly, the system was a 1300 nm fiber-based SD-OCT system using a superluminescent diode with a bandwidth of 170 nm (LS2000B, Thorlabs). The measured axial resolution was 6.0 μm (FWHM) in air. The fiber

core was imaged with a pair of 30 mm focal length doublets (AC254-030-C, Thorlabs) acting as collimator and objective lenses, resulting in an NA of 0.1 (at $1/e^2$) in air. A 1024 pixel InGaAs line-scan camera (SU-LDH2, Goodrich) operated at 92 kHz line rate was used in the spectrometer. The transverse field-of-view consisted of 300x300 pixels^2. Combined with the custom waveform, the effective frame rate was 256 FPS.

Measurements were performed in one of two configurations as pictured in Fig. 4. In the first configuration, the finger was gently pressed on a coverslip glued to a kinematic optics mount (KM100T, Thorlabs) cantilevered out from a 3-axis translation stage (PT3, Thorlabs). In this configuration, there is an air gap between the sample mount and the rest of the sample arm. This allows the sample to move relative to the other sample arm optics. The second configuration is the monolithic (objective-mounted) sample arm design utilized in [38], where a coverslip was mounted on the bottom of the lens tube containing the objective lens, and attached to the galvanometer scanning cube. In this configuration, all optical components and the sample will move together, providing stable *in vivo* imaging. Stability assessments (phase and XCC analyses) of each configuration were performed by placing the stationary beam over a single sweat duct and imaging in an M-mode configuration. This helped to satisfy the assumptions outlined in Section 2.1.

The results are outlined in Fig. 5. The top row [Figs. 5(a)–5(d)] shows representative data from the cantilever-mounted tissue and the middle row [Figs. 5(e)–5(h)] shows representative images obtained with the objective-mounted tissue. Figures 5(c) and 5(d) show the pseudo-*en face* planes from the stability analysis for the cantilever-mounted finger. Large fluctuations can be seen in both the phase and XCC analyses suggesting an unstable system. Quantitatively, for the phase analysis, the fluctuations were $\sigma_{Frame} = 0.47$ radians/frame , and the maximum step along the pseudo-slow axis was 8.45 radians. Assuming a bulk refractive index of 1.44, central wavelength of 1300 nm, and using Eq. (1), this corresponds to physical displacements of 0.79 µm/frame and 0.61 µm, respectively. Referring back to Fig. 4 from Part I of this paper [19], we find that the rapid fluctuations are close to the thresholds for 1-D Brownian motion in the axial dimension, but the large axial steps along the pseudo-slow axis are well above the threshold. This suggests that the reconstruction will show local motion artifacts rather than a global broadening. This effect can be seen in Figs. 5(a) and 5(b) which are OCT and ISAM *en face* planes through a single sweat duct. In the ISAM reconstruction, discrete vertical stripes are visible, resulting from large step-like movements of the tissue. In addition, the strong correlation between the phase and XCC analyses suggests that most of the motion is in the axial direction.
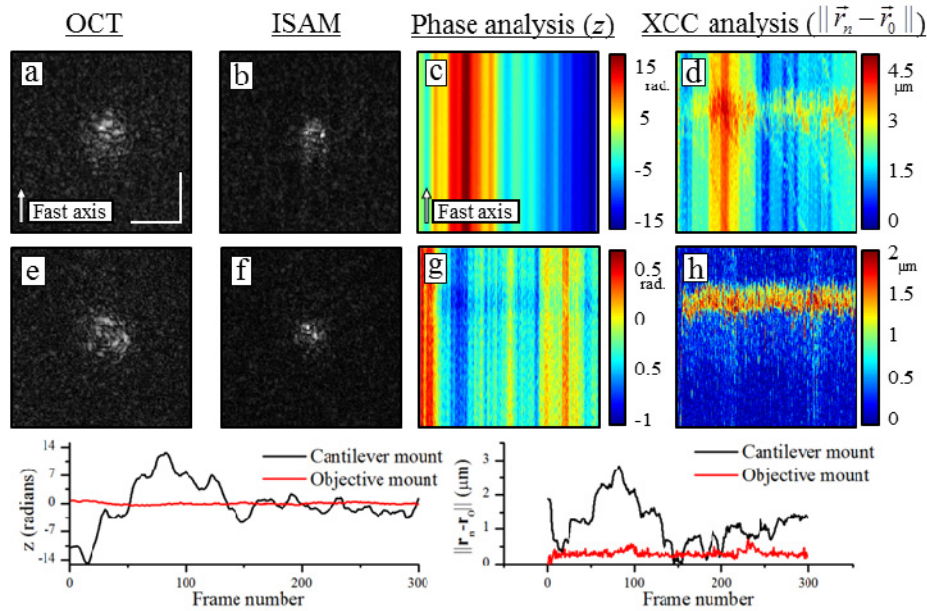
Fig. 5. Stability analysis for *in vivo* tissues. (a-d) Images and stability analysis from a cantilever-mounted finger. The OCT and ISAM reconstructions show *en face* planes through a single sweat duct. The reconstruction in (b) shows motion artifacts due to the large amount of motion, which is also seen in the stability analysis in (c,d). (e-h) Images and stability analysis from an objective-mounted finger. The ISAM reconstruction in (f) is free of motion artifacts due to a much more stable imaging configuration. The smaller motion is also reflected in the stability analysis in (g,h). Scale bars represent 100 μm.

Pseudo-*en face* planes from the stability analysis of the objective-mounted finger data are shown in Figs. 5(g) and 5(h). The range of movement is much lower than that seen in Figs. 5(c) and 5(d) (note the color bars on the right). In addition, an interesting feature is present in the XCC analysis which is not present in the phase analysis. The XCC analysis shows a very flat response, except for a horizontal stripe along the top. Since this stripe does not appear in the phase analysis, it strongly suggests that it results from pure transverse motion. We hypothesize that since it appears at the beginning of each fast-axis frame, it is a system clock causing the galvanometer scanners to temporarily jump. From our XCC measurements, we approximate the amplitude of this jump to be as large as 2 μm which corresponds to 0.22 in relative units (using the transverse resolution of 8.9 μm at $1/e^2$). Referring back to Fig. 4 from Part I [19], a step this large along the fast axis is close to the stability threshold, which can explain why at times artifacts in the ISAM reconstructions resulting from this instability are noticeable (data not shown). In addition, the standard deviation of the phase fluctuations and XCC fluctuations are 0.11 radians/frame and 0.011 frame^{-1} respectively. The absence of any additional large steps (besides what has previously been noted) or sinusoidal fluctuations thus satisfies the stability requirements. OCT and ISAM *en face* planes through a single sweat duct are shown in Figs. 5(e) and 5(f). The lack of reconstruction artifacts support the stability analysis, showing that this configuration is stable enough for *in vivo* imaging.

Finally, the plots at the bottom of Fig. 5 show traces along the pseudo-slow axes for both the cantilever- and objective-mounted stability analyses after any slow linear ramps are fit and subtracted. The higher stability of the objective-mounted system is apparent. In addition, the high degree of correlation between the phase analysis and the XCC analysis for the cantilever-mounted finger suggests that the motion is mostly in the axial dimension.

4. Conclusion

This article provided a stability assessment technique capable of partially decoupling axial from transverse motion, and was specifically aimed at the analysis of *in vivo* phase-sensitive processing methods. The ability to quantitatively analyze the axial motion and transverse motion separately provided insight into the manner in which instabilities arise in the measured data. Furthermore, this assessment could be performed *in vivo* allowing for the important analysis of sample motion. We found that for *in vivo* imaging, the sample mounting configuration could dramatically change the stability of the imaging system. In particular, for the mounting configurations shown here, we found that axial motion impacted the computed imaging reconstructions well before transverse motion. For other imaging scenarios where direct contact cannot be made with the sample, transverse motion may play a more significant role in stability.

As has been discussed previously [39], motion often presents practical tradeoffs between the imaging field-of-view and the required imaging speed (and thus SNR), especially in high-resolution imaging. Using the presented stability assessment technique in conjunction with the stability requirements, this tradeoff can be further explored. Provided the quantitative measure of motion in a particular mounting configuration, the longest interrogation length [19] desired to reconstruct, and the desired square field-of-view, a minimum scan speed could then be determined for successful reconstructions. It is also worth noting that sample motion in addition to other instabilities should be viewed as random processes. This means that one cannot guarantee with 100% confidence that a particular imaging configuration is stable enough for the computed imaging technique. Rather, one must consider the probability that a reconstruction will fail.

Finally, we believe that the quantitative stability analysis provided here can find use in a wide variety of *in vivo* phase-sensitive processing techniques such as Doppler OCT, phase variance OCT, and optical coherence elastography. This also includes the possibility of using these assessment techniques for motion correction.

Acknowledgments